ARTICLES
PUBLISHED ONLINE: 15 AUGUST 2016 | DOI: 10.1038/NMAT4718

nature materials

Mechanism of hard-nanomaterial clearance by the liver

Kim M. Tsoi[1,2†], Sonya A. MacParland[3†], Xue-Zhong Ma[4], Vinzent N. Spetzler[4], Juan Echeverri[4], Ben Ouyang[1], Saleh M. Fadel[3], Edward A. Sykes[1], Nicolas Goldaracena[4], Johann M. Kaths[4], John B. Conneely[4], Benjamin A. Alman[5], Markus Selzner[4], Mario A. Ostrowski[3], Oyedele A. Adeyi[6], Anton Zilman[1,7], Ian D. McGilvray[4*] and Warren C. W. Chan[1,8,9,10,11*]

The liver and spleen are major biological barriers to translating nanomedicines because they sequester the majority of administered nanomaterials and prevent delivery to diseased tissue. Here we examined the blood clearance mechanism of administered hard nanomaterials in relation to blood flow dynamics, organ microarchitecture and cellular phenotype. We found that nanomaterial velocity reduces 1,000-fold as they enter and traverse the liver, leading to 7.5 times more nanomaterial interaction with hepatic cells relative to peripheral cells. In the liver, Kupffer cells (84.8 ± 6.4%), hepatic B cells (81.5 ± 9.3%) and liver sinusoidal endothelial cells (64.6 ± 13.7%) interacted with administered PEGylated quantum dots, but splenic macrophages took up less material (25.4 ± 10.1%) due to differences in phenotype. The uptake patterns were similar for two other nanomaterial types and five different surface chemistries. Potential new strategies to overcome off-target nanomaterial accumulation may involve manipulating intra-organ flow dynamics and modulating the cellular phenotype to alter hepatic cell interactions.

The concept of the 'magic bullet' popularized by Paul Ehrlich describes the design of therapeutic agents that selectively attack pathogens and diseased tissue but leave healthy cells untouched. This idea has inspired the fields of nanotechnology and bioengineering, leading to huge investments in the development of agents to more efficiently diagnose and treat human diseases, such as cancer[1], diabetes[2] and atherosclerosis[3]. Researchers have produced nanoscale materials with unique optical, physical and electrical properties that can encapsulate drugs and/or contrast agents and be coated with homing ligands. *In vitro* studies have shown that nanomaterials are capable of killing and/or imaging cells[4–7]. However, this success has not carried over to human use, largely due to a delivery problem. *In vivo*, the majority of the injected dose is cleared from the bloodstream by cells of the mononuclear phagocyte system (MPS) and most nanomaterials never reach their intended site[8]. The MPS is a network of immune and architectural cells, located in organs such as the liver, spleen and bone marrow, which remove foreign material from the bloodstream. Biodistribution studies have shown this to be the case for all types of nanomaterials—micelles[9,10], quantum dots[11,12], gold nanoparticles[13,14], and carbon nanotubes[15,16]. Accumulation in the MPS is the single biggest hurdle to the clinical translation of nanotechnology because it impedes delivery of a sufficient nanomaterial dose to the disease site and can raise toxicity concerns. Nano-researchers often treat the MPS as a 'blackbox', which has led to a poor understanding of the nanomaterial–MPS interaction and a lack of effective solutions.

Role of organ microarchitecture in clearance

To elucidate the mechanism of nanomaterial clearance, we first analysed accumulation from a whole organ perspective. We used three model hard nanomaterials—quantum dots, gold nanoparticles, and silica nanoparticles—as these materials can be synthesized with a narrow size distribution in the nanoscale (diameter of 1–100 nm) and are amenable to coating with a wide range of functional ligands. Consequently, they permit investigation into the impact of size, composition and surface chemistry on nanomaterial sequestration without the added variables of deformation and degradation that are common for soft nanomaterials such as liposomes, micelles and polymers. We focused on non-degradable, hard nanomaterials, as their physicochemical properties are more likely to remain stable throughout the course of an *in vivo* experiment. In this manner, key design features can be evaluated and the findings can provide a foundation for future experiments that explore additional variables

[1]Institute of Biomaterials and Biomedical Engineering, University of Toronto, Rosebrugh Building, Room 407, 164 College Street, Toronto, Ontario M5S 3G9, Canada. [2]Division of Orthopaedic Surgery, University of Toronto, 149 College Street, Toronto, Ontario M5T 1P5, Canada. [3]Department of Immunology, University of Toronto, Medical Sciences Building, Room 6271, 1 King's College Circle, Toronto, Ontario M5S 1A8, Canada. [4]Multi Organ Transplant Program, Toronto General Research Institute, University Health Network, 200 Elizabeth Street, Toronto, Ontario M5G 2C4, Canada. [5]Department of Orthopaedic Surgery, Duke University, Duke University Medical Center, Room 2888, 200 Trent Drive, Durham, North Carolina 27710, USA. [6]Department of Pathology, Toronto General Hospital, 200 Elizabeth Street, Toronto, Ontario M5G 2C4, Canada. [7]Department of Physics, University of Toronto, 60 St. George Street, Toronto, Ontario M5S 1A7, Canada. [8]Terrence Donnelly Centre for Cellular and Biomolecular Research, University of Toronto, 160 College Street, Room 230, Toronto, Ontario M5S 3E1, Canada. [9]Department of Chemical Engineering, University of Toronto, 200 College Street, Toronto, Ontario M5S 3E5, Canada. [10]Department of Chemistry, University of Toronto, 80 St George Street, Toronto, Ontario M5S 3H6, Canada. [11]Department of Material Science and Engineering, University of Toronto, 160 College Street, Room 450, Toronto, Ontario M5S 3E1, Canada. [†]These authors contributed equally to this work. *e-mail: Ian.McGilvray@uhn.ca; warren.chan@utoronto.ca

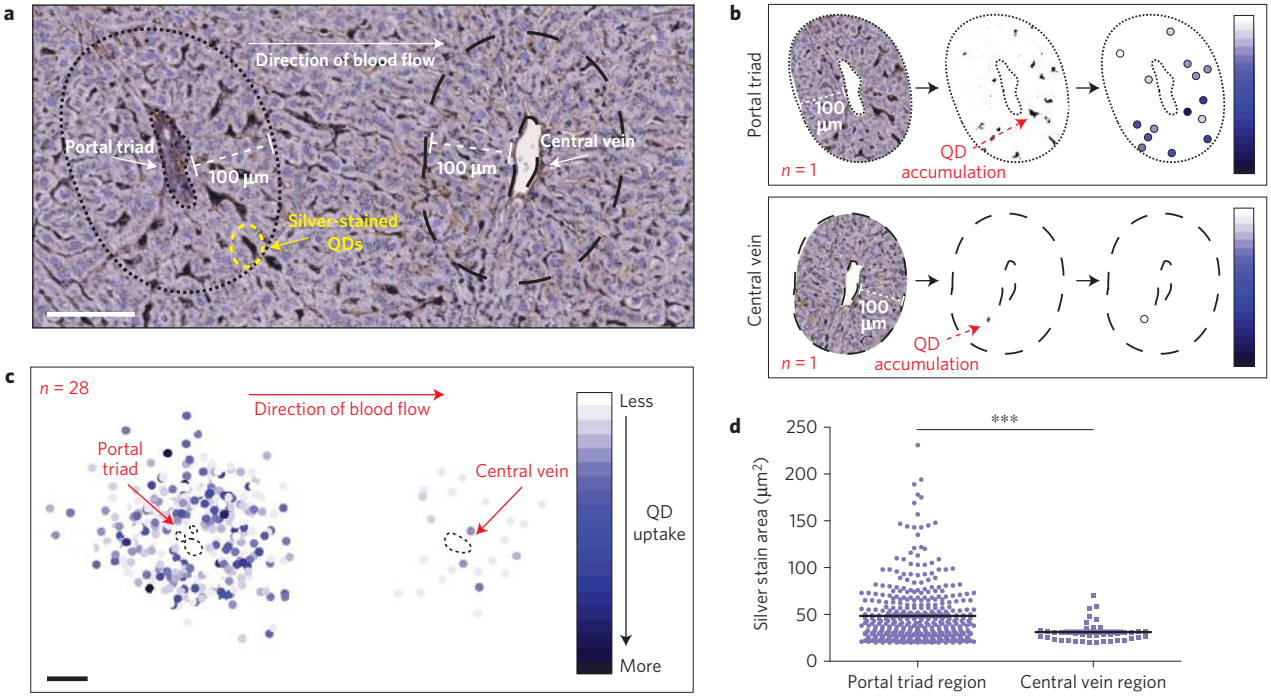

Figure 1 | Distribution of quantum dots in the liver following systemic intravascular injection. a, Silver-stained section of a rat liver that was perfused 4 h post-quantum-dot-injection (counterstained with haematoxylin). One repeating unit of the liver microarchitecture is shown. Blood flows into the liver via the hepatic artery and portal vein, which are located in the portal triad. Blood flows out of the liver via the central vein. A zone with a radial distance of 100 µm was traced around each vascular unit. Scale bar, 100 µm. **b**, Overview of the image processing used to measure quantum dot accumulation in the zones bordering the portal triad and central vein. First, the zone surrounding each vascular structure was extracted using a radius of 100 µm from the vessel border. Second, the image was converted into a binary format and thresholded to isolate reduced silver. Finally, the area of each silver stain was measured along with its (x, y) coordinates relative to the centre of the vessel. The area of reduced silver corresponds to the amount of quantum dot accumulation and is represented by a colour spectrum, where pale blue indicates a small amount of quantum dot accumulation and dark blue indicates a large amount of quantum dot accumulation in each individual location. **c**, Twenty-eight portal triad–central vein pairs were analysed and the results combined. Scale bar, 100 µm. **d**, Scatter plot comparing the area of each region of silver staining in the zone surrounding the portal triad versus in the zone surrounding the central vein. The data plotted here are the same as displayed in **c**. Statistical significance was evaluated using a two-tailed unpaired *t*-test (***$P < 0.001$). Additional portal triad–central vein pairs are included in Supplementary Fig. 4.

to ultimately define a general mechanism of liver sequestration for all hard and soft nanomaterials. In the first set of experiments, fluorescent quantum dots (see Supplementary Fig. 1) were administered to Wistar rats, and after 4 h the liver was silver stained to visualize the nanomaterial with bright-field microscopy. A dose of 14 µg quantum dots per gram body weight was chosen because it is comparable to recent studies[12,17] and did not result in toxicity (see Supplementary Figs 2 and 3). We observed a higher amount of quantum dot accumulation in the zone surrounding the portal triad than in the zone surrounding the central vein. Twenty-eight portal triad–central vein pairs were analysed (see Fig. 1a,b and Supplementary Fig. 4) and we found both more (410 versus 42) and larger ($48.5 \pm 31.5\,\mu m^2$ versus $31.2 \pm 10.8\,\mu m^2$) areas of quantum dot accumulation in the portal triad zone than in the central vein zone (see Fig. 1c,d). The same trend was found to apply to gold nanoparticles, irrespective of surface chemistry; preferential peri-portal accumulation was observed for nanoparticles coated with poly(ethylene glycol) or with the cancer-targeting ligand transferrin (see Supplementary Figs 5–8). Interestingly, the data also showed the importance of protein adsorption in mediating cellular sequestration (6 PEG nm^{-2} coating versus 0.25 PEG nm^{-2} or low versus high amounts of protein adsorption). Nanomaterial designs that experience high protein adsorption are taken up significantly more by peri-portal cells than designs with low protein adsorption (see Supplementary Figs 6–8 and Supplementary Methods 1). From these studies, two patterns emerge relating to intra-organ nanomaterial uptake. First, a cell located near the vascular inlet is more likely to take up a nanomaterial, and second, this cell will accumulate more nanomaterial when compared to a cell located near the vascular outlet. In addition, the degree with which peri-portal cells sequester hard nanomaterials is related to the amount of protein adsorption. These results highlight the importance of microarchitecture in mediating nanomaterial uptake by the liver.

Role of flow dynamics in clearance

Within the liver microarchitecture, blood flow is significantly slower than in the systemic circulation. In arteries and veins, nanomaterials travel at velocities of 10–100 cm s^{-1} (refs 18–20), but slow down to 200–800 µm s^{-1} when they enter a liver sinusoid[21,22]. We hypothesized that the reduced velocity promotes preferential nanomaterial accumulation within the sinusoid. If we assume that nanomaterials are taken up by MPS cells residing on vessel walls then, heuristically, body sites with lower blood velocities will have more nanomaterial accumulation. This is because a nanomaterial will have a high chance of reaching the wall by diffusion before exiting the vessel by advection. To explore this theory, we developed a mathematical model describing the process of nanomaterial sequestration by cells. Sequestration is defined as any removal of a nanomaterial from circulation due to its interaction with a cell, and includes both binding to the cell surface and internalization into the cell cytoplasm. The vessel was modelled as a cylindrical channel of length, L, and radius, r_o, with a flow velocity profile, $v(r)$, and cells were assumed to reside on vessel walls (see Fig. 2a). Nanomaterial sequestration was modelled using an absorbing or

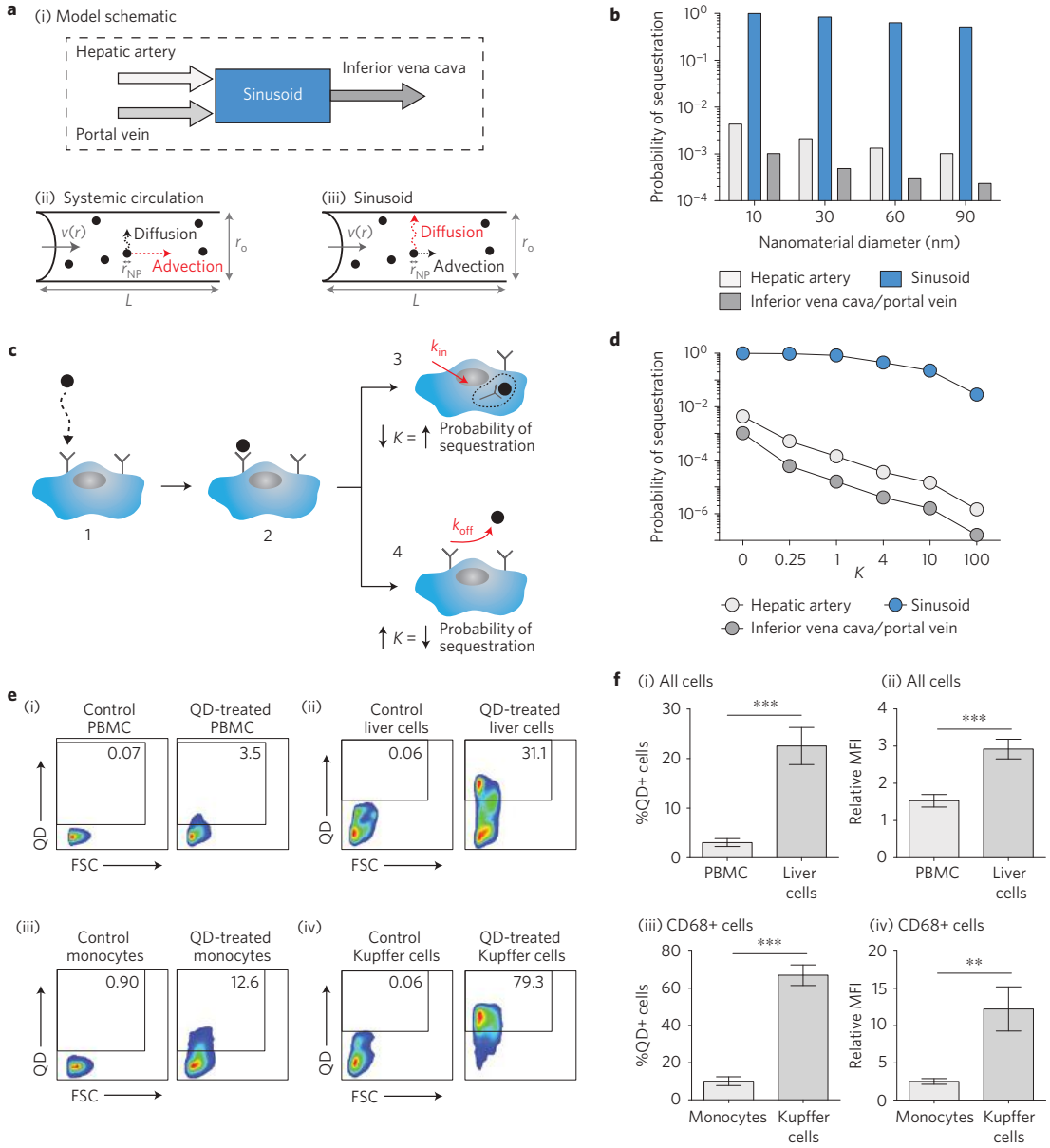

Figure 2 | Nanomaterial sequestration in the liver versus in the systemic circulation: mathematical modelling and *in vivo* results. a, (i), Model schematic. (ii), In the systemic circulation (for example, hepatic artery, portal vein, inferior vena cava), advection due to blood flow is the dominant factor influencing nanomaterial transport. (iii), In the liver sinusoid, diffusion due to Brownian motion is the dominant factor influencing nanomaterial transport. **b**, Results of the mathematical model comparing the probability of a nanomaterial being sequestered in a liver sinusoid versus in the systemic circulation. An absorbing boundary condition on the vessel wall was utilized. The impact of nanomaterial size, between 10 and 90 nm, is shown. Numerical inputs to the model are included in Supplementary Table 1. **c**, The impact of imperfect adsorption was incorporated in the local sticking coefficient, K, where $K \propto k_{off}/k_{in}$. In the illustration, a nanomaterial reaches a cell by Brownian motion (1) and may bind to a cell receptor (2). There are then two possible scenarios. In 3, the nanomaterial has a higher probability of internalization into the cell cytoplasm, decreasing K and increasing the overall probability of sequestration. Alternatively, in 4, the nanomaterial has a higher probability of dissociation into the circulation, increasing K and decreasing the overall probability of sequestration. **d**, Results of the mathematical model probing the impact of varying values of K on the overall probability of sequestration in the systemic circulation and in the liver sinusoid for a 10 nm nanomaterial. The impact of K on 30/60/90 nm nanomaterials is included in Supplementary Fig. 9. **e**, Representative flow plots comparing quantum dot uptake *in vivo* by cells in the peripheral blood (i, iii) versus in the liver (ii, iv) 12 h post-injection. The first comparison is for all peripheral blood mononuclear cells (PBMCs, i) versus all cells in the total liver homogenate (ii). The full gating strategy is included in Supplementary Fig. 10. The second comparison is for CD68+ monocytes (iii) with CD68+ Kupffer cells (iv). Plots from the control vehicle-treated animal (Control), and the quantum-dot-treated animal (QD-treated) are shown. The full gating strategy for uptake in CD68+ cells is included in Supplementary Fig. 16A. The gates (boxes) highlight the nanoparticle-positive cells and the gates are set based on the nanoparticle untreated fully-stained controls. **f**, Percentage of quantum-dot-positive cells in the peripheral blood versus in the liver 12 h after intravenous quantum dot injection (i, iii), where $\%QD+\ cells = \%QD+\ cells_{QD\text{-}treated} - \%QD+\ cells_{Control\text{-}treated}$. In (i) the quantum dot uptake in all PBMCs is compared with uptake in all total liver homogenate cells. In (iii) the quantum dot uptake in monocytes is compared with uptake in Kupffer cells. The amount of quantum dot uptake for each cell type, where relative mean fluorescence intensity or relative $MFI = MFI_{QD\text{-}treated}/MFI_{Control\text{-}treated}$ (ii, iv). Again, in (ii) the comparison is made for all cells, whereas in (iv) the comparison is made for CD68+ cells (monocytes versus Kupffer cells). The mean ± s.e.m. from eight independent replicates are plotted. Statistical significance was evaluated using a two-tailed unpaired t-test ($^{**}P < 0.01$, $^{***}P < 0.001$).

partially absorbing boundary condition on the channel walls. The density $c(z,r,t)$ of the nanomaterial inside the channel could then be described by the following equation[23,24]:

$$\frac{\partial}{\partial t}c(r,z,t)+v(r)\frac{\partial}{\partial z}c(r,z,t)=D\frac{1}{r}\frac{\partial}{\partial r}\left(r\frac{\partial}{\partial r}c(r,z,t)\right)+\frac{\partial^2}{\partial z^2}c(r,z,t) \quad (1)$$

The two principal factors that influence nanomaterial transport within a vessel—flow along the longitudinal axis (advection) and Brownian motion along the radial axis (diffusion) are represented by the second term on the left and the first term on the right, respectively. For a spherical nanomaterial of diameter, d_{NP}, the diffusion coefficient is $D=(k_B T)/(3\pi\eta d_{NP})$, where D is the nanomaterial diffusion coefficient in the channel, k_B is the Boltzmann constant, T is the physiological temperature and η is the plasma viscosity.

Equation (1) can be solved to yield the probability of nanomaterial sequestration during its passage through the channel:

$$P=\sum_{i=1}^{\infty}\left[1-\exp\left(-\frac{DL}{Ur_0^2}\lambda_i\right)\right]b_i \quad (2)$$

where U is the average flow velocity and b_i and λ_i are numerical coefficients. The sequestration probability, P, is a decreasing function of the dimensionless parameter $(Ur_0^2)/(DL)$, which measures the strength of advection relative to diffusion. Using values derived empirically and from the literature, we compared the computationally predicted probability of nanomaterial sequestration in two different locations: the liver sinusoid and the systemic circulation (see Supplementary Table 1). The liver inlet (hepatic artery, portal vein) and outlet (inferior vena cava) were selected as representative of the systemic circulation. For a Poiseuille parabolic flow profile with fully absorbing walls, the model predicts a 10^2–10^3 times greater probability of nanomaterial sequestration in a liver sinusoid than in the extra-hepatic circulation (see Fig. 2b). As many types of flow occur *in vivo*, we tested the model's robustness by replacing the parabolic flow assumption with a flat flow profile. The prediction of higher nanomaterial sequestration within the sinusoid persists; however, the difference between regions is reduced (see Supplementary Fig. 9). This finding extends to other types of flow, as the shape of the flow profile $v(r)$ in equation (2) does not alter the expression for the sequestration probability P, only the numerical values of the coefficients, b_i and λ_i. To validate our mathematical model and experimentally test our hypothesis, we isolated hepatic and peripheral blood mononuclear cells (PBMCs) from the quantum-dot-treated rats and determined nanomaterial uptake via flow cytometry. As predicted by the model, hepatic cells took up significantly more quantum dots than did PBMCs. The trend persisted when we looked specifically at cells in the monocyte–macrophage lineage (CD68+ cells), as 67.1 ± 15.7% of Kupffer cells and only 10.0 ± 6.3% of monocytes were quantum-dot-positive (see Fig. 2e,f and Supplementary Fig. 10). The importance of flow dynamics is reinforced by the fact that, under static culture conditions, monocytes took up quantum dots with the same affinity as Kupffer cells (see Supplementary Figs 11 and 12).

Nanomaterials that bind to a cell can remain on its surface, or return to the circulation or be internalized through receptor-mediated endocytosis, phagocytosis or pinocytosis[25–27]. To take nanomaterial–cell interactions into account, a parameter, K, was added to the model, which quantifies the local sticking coefficient and combines factors that affect nanomaterial binding to and internalization into a cell: cell density on the vessel wall, receptor density on the cell surface, internalization rate (k_{in}) and dissociation rate (k_{off}). K is proportional to k_{off}/k_{in} and varies from infinity for a completely reflective surface to zero for a completely absorbing one (see Fig. 2c). The value of K therefore depends on nanomaterial design, serum protein adsorption and cellular phenotype. The trend of preferential nanomaterial sequestration in the liver compared with the systemic circulation is magnified when incomplete absorption due to nanomaterial–cell interactions is considered. For a 10 nm nanomaterial and an intermediate K of 4, the probability of sequestration in the sinusoid is 10^4 times higher than in the hepatic artery. If complete absorption is assumed, the difference is 50-fold less (see Fig. 2d and Supplementary Fig. 9).

Role of nanomaterial size and surface chemistry

We next investigated the contribution of blood flow dynamics to the size-dependent clearance of nanomaterials from circulation. We calculated the predicted effect of nanomaterial diameter, d_{NP}, on the probability of nanomaterial sequestration using equation (2). The model suggests that modifying the particle diameter between 10 and 90 nm does not significantly influence the probability of sequestration compared to the impact of vessel radius or blood velocity (see Fig. 2b). The probability of sequestration for a 10 nm nanomaterial is twice as high as for a 90 nm nanomaterial within the sinusoid. Contrastingly, the same 10 nm nanomaterial is 1,000 times less likely to be sequestered in the extra-hepatic circulation than in the sinusoid. However, many studies show that larger nanomaterials are preferentially cleared by the liver[28–30]. This suggests a second contribution to nanomaterial clearance: the macrophage's propensity to phagocytose larger nanomaterials. Using fluorescent gold nanoparticles (see Supplementary Fig. 5), we show that both primary rat Kupffer cells and immortalized murine macrophages preferentially took up larger nanoparticles (see Supplementary Figs 13 and 14). This phenomenon, reported for multiple nanomaterial types (see Supplementary Table 2), may be attributable to the higher surface ligand density present on larger nanomaterials. Higher ligand density permits a multivalent receptor–ligand interaction between the cell and nanomaterial, and is therefore more likely to lead to uptake[31,32]. Thus, nanomaterial surface chemistry does not necessarily contribute to the probability of cellular interaction, but does influence how long a nanomaterial remains bound to the cell surface and whether it is internalized. A future study that investigates the role of specific adsorbed proteins in cellular binding and phagocytosis is required to fully understand sequestration.

Intra-hepatic cellular interaction

Our first set of studies provided an organ-level view of nanomaterial clearance. We then proceeded to analyse sub-organ biodistribution. The prevailing assumption is that Kupffer cells are responsible for nanomaterial uptake by the liver; however, we hypothesized that a variety of hepatic cell types would internalize nanomaterials due to favourable flow dynamics in this organ. We deconstructed the nanomaterial–liver interaction by characterizing the distribution of quantum dots in hepatic cells at two timepoints following systemic nanomaterial administration (see Fig. 3a and Supplementary Figs 15–17). Our results demonstrate that 12 h post-injection 84.8 ± 6.4% of Kupffer cells, 81.5 ± 9.3% of B cells, 64.6 ± 13.7% of endothelial cells, along with a much smaller percentage of T cells and an 'other' population (CD19-, CD31- and CD68-negative mononuclear cells), took up the quantum dots (see Fig. 3b and Supplementary Fig. 18). Quantum dots were not detected in hepatocytes (see Fig. 3a and Supplementary Fig. 16). This finding is in contrast to studies suggesting that hepatocytes accumulate certain nanomaterials[33,34], potentially via the acquisition of ApoE from serum[35]. Interestingly, there was no difference in the percentage of quantum-dot-positive cells between the four- and

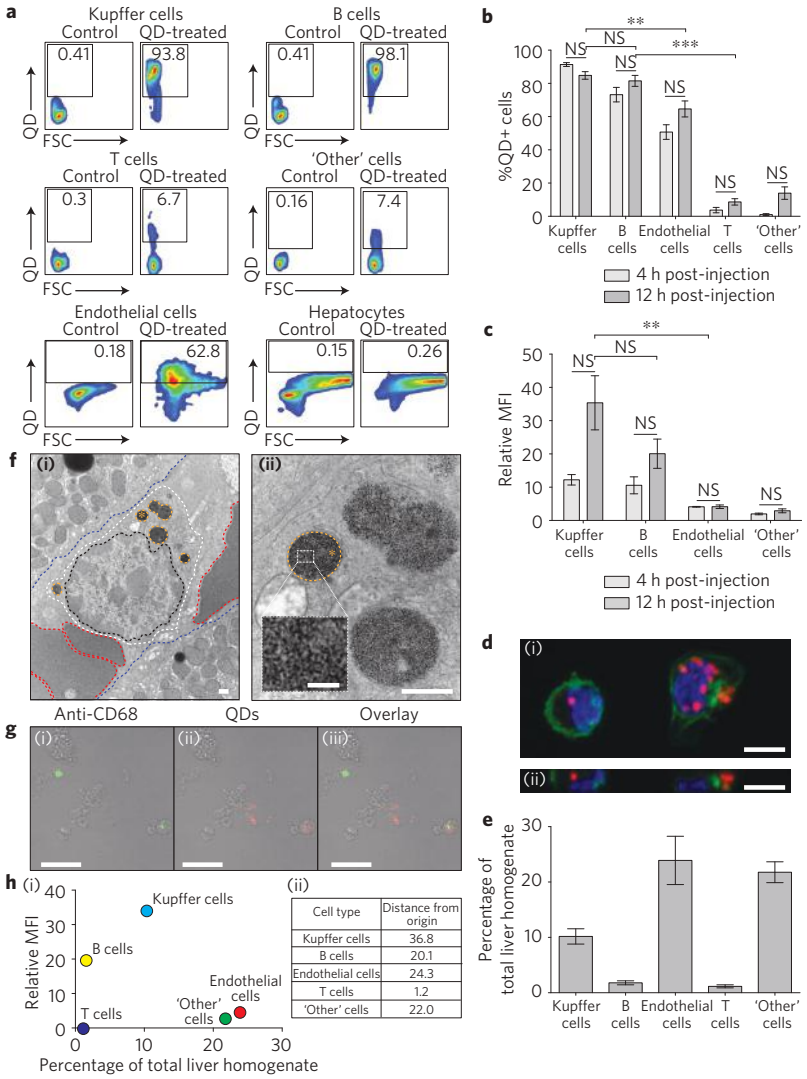

Figure 3 | Characterization of *in vivo* quantum dot uptake in the liver. a, Representative flow plots illustrating quantum dot uptake in hepatic cell populations 12 h post-injection. The full gating strategy is included in Supplementary Figs 15–17. Representative flow plots for the 4 h timepoint are included in Supplementary Fig. 19. **b**, Percentage of each hepatic cell type that is quantum-dot-positive at the 4 and 12 h. **c**, The amount of quantum dot uptake for each hepatic cell type at the 4 and 12 h. **d**, Confocal microscopy images demonstrating the intracellular location of quantum dots. A *z*-stack image of cells from the Kupffer cell-enriched fraction (i) and an orthogonal projection in the *y*–*z* plane (ii) are shown. The nucleus is stained with Hoechst 33342 (blue), actin is stained with Alexa Fluor 488-labelled phalloidin (green), quantum dots are red. Images were acquired with a ×60 PlanApo oil objective (NA 1.4) with the following excitation (ex) and emission (em) wavelengths: nuclei ($\lambda_{ex}=405$ nm; $\lambda_{em}=442/35$ nm); actin ($\lambda_{ex}=473$ nm; $\lambda_{em}=515/60$ nm); quantum dots ($\lambda_{ex}=559$ nm; $\lambda_{em}=598/45$ nm). Scale bars, 5 μm. **e**, Relative prevalence of hepatic cell types reported as a percentage of the total cells in the liver homogenate. The full gating strategy is included in Supplementary Fig. 21. For **b**,**c** and **e**, the mean ± s.e.m. from at least six independent replicates for the 12 h timepoint and three independent replicates for the 4 h timepoint are plotted. Statistical significance was evaluated using a two-tailed unpaired *t*-test (**$P<0.01$, ***$P<0.001$, NS = not significant or $P>0.05$). **f**, Transmission electron microscopy images demonstrating the presence of quantum dots within peri-nuclear membrane-bound structures in a hepatic lymphocyte-like cell 12 h post-injection. Images of a Kupffer-like cell and an endothelial-like cell are included in Supplementary Fig. 20. (i), The location of the cell within the sinusoid, the lymphocyte plasma membrane is traced in white, the nucleus in black and the quantum-dot-containing membrane-bound intracellular vesicles in yellow. (ii), For orientation, red blood cells are traced in red and hepatocytes in blue. A high-resolution image of the quantum-dot-containing vesicles, the asterisk marks corresponding structures. The inset demonstrates individual quantum dots. Scale bars in (i) and (ii), 500 nm. Scale bar in inset, 100 nm. **g**, Confocal images demonstrating anti-CD68 staining in quantum-dot-positive and -negative cells. Cells from the Kupffer cell-enriched fraction of a quantum-dot-treated animal were stained with an Alexa Fluor 647-labelled anti-CD68 antibody. (i)–(iii), Antibody staining only (i), quantum dot uptake only (ii) and an overlay of both channels (iii). The anti-CD68 antibody is green, quantum dots are red and co-staining is yellow. Images were acquired with a ×60 PlanApo oil objective (NA 1.4), a zoom of ×1.4 with the following excitation wavelengths: quantum dots ($\lambda_{ex}=559$ nm; $\lambda_{em}=598/45$ nm) and anti-CD68 ($\lambda_{ex}=635$ nm; $\lambda_{em}=705/100$ nm). Images were overlayed and pseudo-colour assigned in ImageJ. Scale bars, 30 μm. **h**, The relative importance of each hepatic cell type to quantum dot uptake in the liver as measured by the distance from origin, where: Distance from origin $=\sqrt{(\text{Relative MFI})^2+(\%\text{Total liver homogenate})^2}$. Hepatocytes are not represented, as quantum dot uptake was not detected.

twelve-hour timepoints. Although there was a trend for higher per cell uptake of quantum dots at 12 h, the difference was not statistically significant (see Fig. 3b,c and Supplementary Fig. 19). Confocal and transmission electron microscopy confirmed that quantum dots were intracellular and located in membrane-bound peri-nuclear structures (see Fig. 3d,f and Supplementary Fig. 20).

Immunofluorescence staining was performed to further validate our flow cytometry findings (see Fig. 3g). The uptake data confirms our hypothesis, although we had not anticipated the extent to which B cells internalize nanomaterials. B cells contained a comparable amount of quantum dots to Kupffer cells, a cell type known to avidly phagocytose nanomaterials[12,34,36,37] (see Fig. 3b). Kupffer cells had a relative MFI of 35.4 ± 23.0 while B cells had a relative MFI 20.1 ± 11.6 at 12 h post-injection (see Fig. 3c). Although hepatic B cells have been shown to internalize microparticles[38], their role in nanomaterial clearance has not previously been described. Endothelial and 'other' cells were more weakly positive with relative MFI values of 4.1 ± 1.5 and 2.9 ± 1.6, respectively (see Fig. 3c). Interestingly, the distribution of quantum-dot-positive cells was different from that of the population distribution of liver cells. Endothelial and the 'other' cells were measured to be the most abundant (23.9 ± 16.3% and 21.8 ± 7.1%, respectively), followed by Kupffer cells (10.2 ± 5.2%), and finally B cells (1.8 ± 1.4%) (see Fig. 3e and Supplementary Fig. 21). We verified that quantum dot exposure did not result in cellular recruitment to the liver (see Supplementary Fig. 22). Combining the parameters of relative MFI and % total liver homogenate allowed us to determine the most important liver cell types involved in nanomaterial sequestration. Kupffer cells play the largest role in removing quantum dots from circulation, while endothelial cells, B cells, and the 'other' cell type contribute comparably to the process (see Fig. 3h). Having identified hepatic cell types responsible for quantum dot clearance, we wondered whether our findings would extend to other hard-nanomaterial designs. To efficiently screen a range of nanomaterials, we first established that *in vitro* nanomaterial uptake by plated primary rat hepatic cells mirrors patterns observed *in vivo*. Specifically, we show that, both *in vitro* and *in vivo*, quantum dot accumulation is comparable between Kupffer cells and hepatic B cells and that both cell types take up significantly more of this nanomaterial than do T cells (see Supplementary Figs 11 and 23). We then measured uptake of five different designs of gold and silica nanoparticles *in vitro*, assuming that patterns would be reflective of *in vivo* behaviour. We found that, as for quantum dots, multiple hepatic cell types mediated uptake of the tested nanomaterials, but that their relative importance varied with nanomaterial physicochemical properties (see Supplementary Fig. 24).

Influence of cellular phenotype

Finally, we asked whether flow dynamics and microarchitecture could be used to predict nanomaterial uptake in the spleen. We found that nanomaterial accumulation reflects blood velocity, as almost all nanomaterials were found within the red pulp region (see Fig. 4a). Washout studies have demonstrated that blood preferentially slows down in the red pulp, where it has a half-life of ∼10 min (refs 39,40). Like the hepatic sinusoid, the red pulp is rich in macrophages (see Supplementary Fig. 25). As macrophages in the hepatic sinusoid and the splenic red pulp are exposed to nanomaterial-containing blood flowing at a very slow rate, we hypothesized that quantum dot uptake would be comparable between the two macrophage types. However, when we analysed quantum dot uptake in splenic mononuclear cells isolated from quantum-dot-treated rats, we found that splenic macrophages took up significantly less nanomaterial than Kupffer cells. 12 h post-injection, only 25.4 ± 10.1% of splenic macrophages were quantum-dot-positive, compared to 84.8 ± 6.4% of Kupffer cells (see Fig. 4b,c and Supplementary Figs 16 and 26). Splenic macrophages also took up ten times less nanomaterial on a per cell basis (see Fig. 4b,c). A similar trend was seen 4 h post-injection (see Fig. 4c and Supplementary Fig. 27). This suggests that cellular phenotype within the MPS also contributes to uptake. Despite similar opportunity, splenic macrophages have less endocytic/phagocytic affinity for nanomaterials than their counterparts in the liver. We confirmed the role of cellular phenotype by comparing quantum dot uptake by primary splenic and hepatic macrophages *in vitro*. As anticipated, Kupffer cells took up more quantum dots than did splenic macrophages (see Fig. 4d,e and Supplementary Figs 11 and 28). At the 80 nM dose, 59.9 ± 9.0% of Kupffer cells were quantum-dot-positive, compared to 35.1 ± 10.4% of splenic macrophages and the MFI for Kupffer cells was approximately double that for splenic macrophages. The same trend was found for other nanomaterial designs (see Supplementary Fig. 29). Interestingly, the liver–spleen difference is more pronounced *in vivo*, and this may relate to other anatomical and physiological differences between the organs. First, despite their location in the 'slow flow' red pulp region of the spleen, splenic macrophages may not have the same access to transiting nanomaterials as do Kupffer cells in the liver. Second, the rat liver receives approximately 21% of the cardiac output via both the hepatic artery and the portal vein, whereas the spleen receives only 1% via the splenic artery[18,41].

New strategies to reduce liver sequestration

At present, the standard practice for reducing nanomaterial accumulation in the MPS is to focus on nanomaterial design. Researchers manipulate nanomaterial dimensions and also coat the surface with anti-fouling polymers to reduce serum protein absorption[42]. Despite using a small nanomaterial shielded with poly(ethylene glycol), the most commonly used anti-fouling polymer, significant accumulation in the liver occurred, demonstrating that alteration of nanomaterial physicochemical properties will not single-handedly solve the MPS and delivery problem. Our study suggests that manipulation of the host environment should be pursued as a complementary strategy. On the basis of our results, two potential approaches are: increasing the liver flow rate to decrease the probability of nanomaterial sequestration and altering the phenotype of key cells to reduce their affinity for nanomaterials. We tested the feasibility of these approaches in two additional sets of experiments. First, we investigated the relationship between nanomaterial flow rate and uptake by primary rat Kupffer cells. Using standard culture techniques and a microfluidic channel system, we compared quantum dot uptake by Kupffer cells under three conditions: 'static' (0 ml min^{-1}), 'fast' flow (8 ml min^{-1}), and 'slow' flow (0.6 ml min^{-1}) (see Fig. 5a). As anticipated, increasing the flow rate reduced quantum dot uptake. Under static conditions, 48.1 ± 8.9% of Kupffer cells were quantum-dot-positive. This reduced to 16.2 ± 2.5% quantum-dot-positive cells under 'slow' flow conditions, and even further to 8.4 ± 2.9% under 'fast' flow conditions (see Fig. 5b,c). These results demonstrate that modulating flow dynamics is a feasible strategy for reducing nanomaterial clearance by phagocytic cells. We next evaluated whether Kupffer cell phenotype could be modified to reduce nanomaterial uptake. For these experiments, we opted to use human rather than rat cells to enhance the clinical relevance of our findings, and isolated Kupffer cells from the resected caudate lobes of livers used for transplantation. Kupffer cells were either left untouched or stimulated with a cytokine cocktail[43] before incubation with the nanomaterial. Uptake of fluorescent gold nanoparticles was reduced by an average of 37% by immune modulation (see Fig. 5d,e). We therefore suggest that manipulating cellular phenotype is a viable strategy to reduce nanomaterial uptake by macrophages. Techniques to alter both hepatic sinusoidal blood velocity and macrophage phenotype *in vivo* have been reported[44,45], and consequently we believe that these two novel approaches are appropriate for in-depth investigation in the future.

Mechanism of hard-nanomaterial clearance by the liver

Putting the modelling and experimental results together, we propose the following mechanism for the sequestration of hard nanomaterials by the liver (see Fig. 6). First, nanomaterials

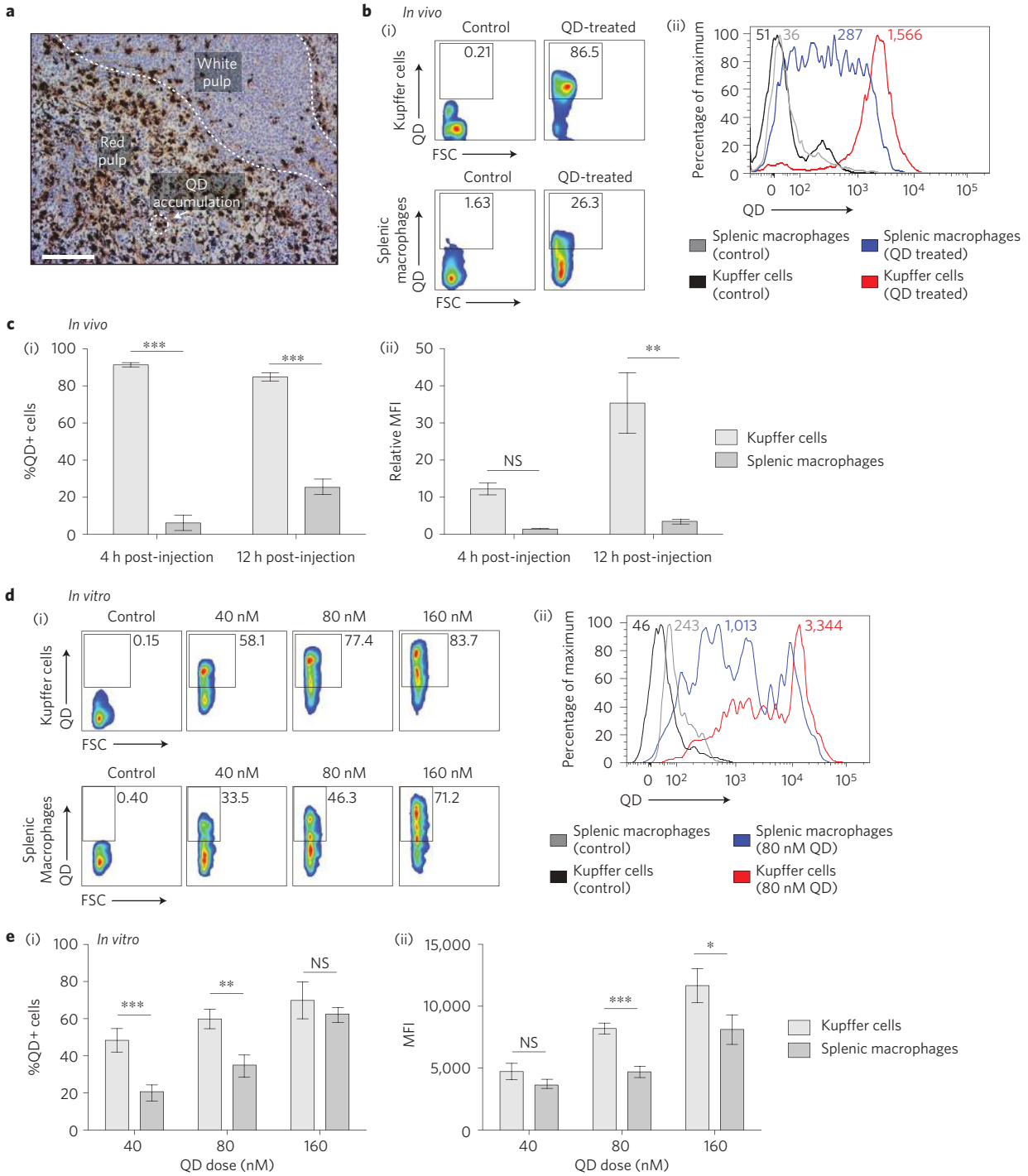

Figure 4 | *In vivo* and *in vitro* results for quantum dot uptake in the liver versus in the spleen. a, Quantum dot uptake in the spleen occurs primarily in the red pulp. Quantum dots are identified via silver staining (haematoxylin counterstain). Scale bar, 100 μm. **b**, (i), Representative flow plots demonstrating the difference in quantum dot uptake between Kupffer cells and splenic macrophages 12 h post-injection. (ii), Corresponding histograms showing the MFI. The full gating strategy is included in Supplementary Fig. 16. Representative flow plots from the four-hour timepoint are included in Supplementary Fig. 27. **c**, (i), Percentage of quantum-dot-positive Kupffer cells and splenic macrophages 4 and 12 h post-injection. (ii), The amount of quantum dots taken up by both cell types. The mean ± s.e.m. from at least six independent replicates for the 12 h timepoint and three independent replicates for the 4 h timepoint are plotted. Statistical significance was evaluated using a two-way analysis of variance (ANOVA) with a Bonferroni post-test (** $P < 0.01$, *** $P < 0.001$, NS = not significant or $P > 0.05$). **d**, (i), Representative flow plots identifying quantum-dot-positive Kupffer cells and splenic macrophages. Isolated cells were either left untreated or incubated with 40/80/160 nM quantum dots. Four incubation times were investigated; the 6 h timepoint is shown. The full gating strategy is included in Supplementary Fig. 11. (ii), Representative histograms showing the MFI in the QD channel at the baseline and after a six-hour incubation with 80 nM quantum dots. **e**, (i), (ii), Percentage of quantum-dot-positive cells (i) and the amount of quantum dot uptake (MFI, ii) for each cell type 6 h post-incubation with 40 nM/80 nM/160 nM quantum dots. %QD+ Cells = %QD+ $\text{Cells}_{\text{QD-Treated}}$ − %QD+ $\text{Cells}_{\text{Untreated}}$. The full time course is included in Supplementary Fig. 28. The mean ± s.e.m. from three independent replicates is plotted. Statistical significance was evaluated using a two-way ANOVA with a Bonferroni post-test for the complete time course (* $P < 0.05$, NS = not significant or $P > 0.05$).

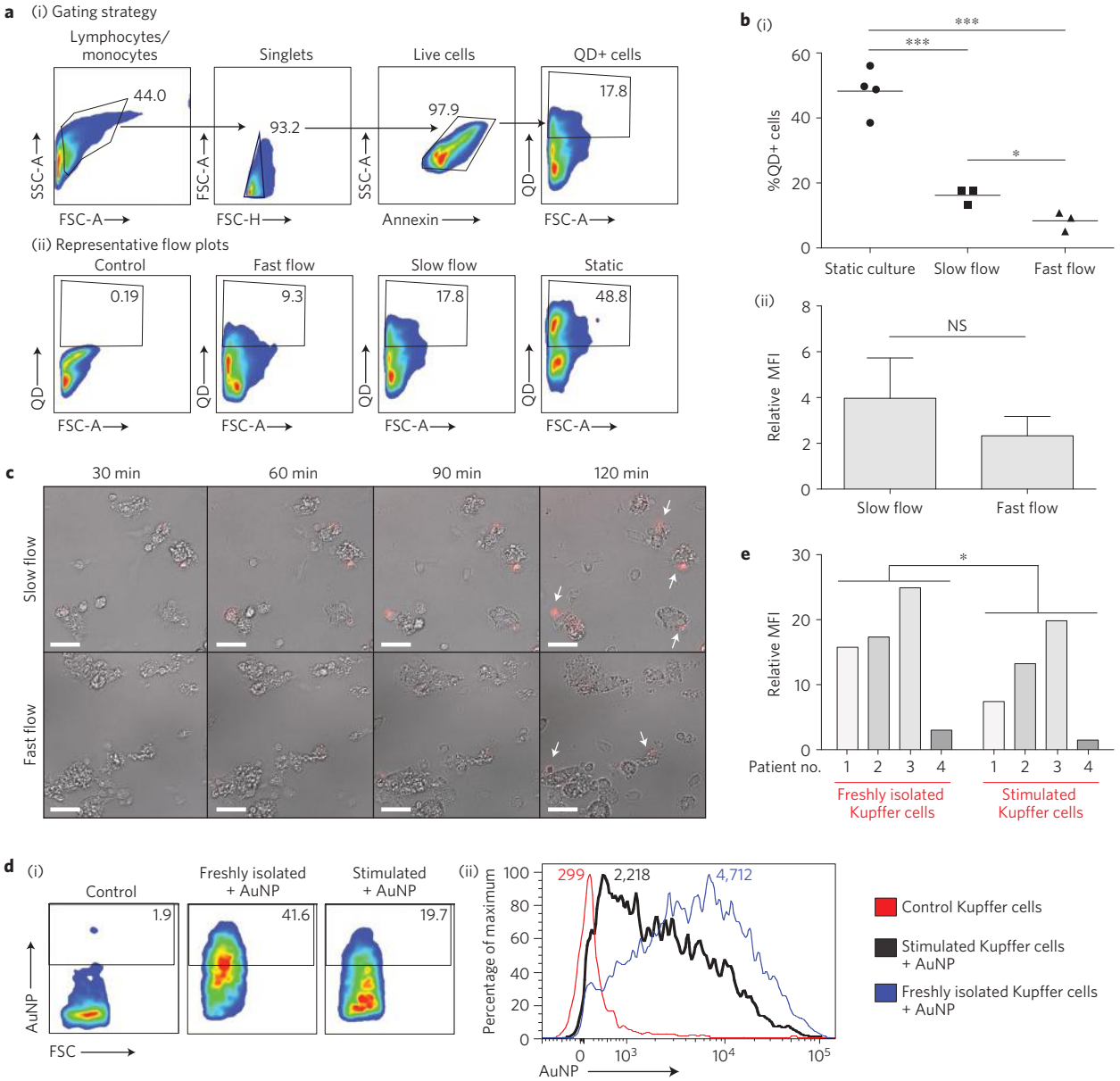

Figure 5 | Nanomaterial uptake by Kupffer cells can be reduced by manipulating flow rate and cellular phenotype. Quantum dot uptake by primary rat Kupffer cells was compared under three conditions: traditional cellculture in a Petri dish (static) or in a microfluidic chip with two different flow rates, fast flow at 8 ml min^{-1} and slow flow at 0.6 ml min^{-1}. **a**, (i), (ii), Flow cytometry plots demonstrating the gating strategy (i) and representative plots showing differences in uptake between static, fast and slow flow conditions (ii). **b**, (i), The percentage of quantum dot-positive, Annexin-negative (that is, live) Kupffer cells under the three conditions. (ii), The amount of quantum dots taken up by Kupffer cells in each: The mean ± s.e.m. from three independent replicates is plotted. Statistical significance was evaluated using a two-tailed unpaired *t*-test (*$P<0.05$, **$P<0.01$, NS = not significant or $P>0.05$). **c**, Time-lapse images comparing uptake under slow and fast flow conditions. Quantum dots are shown in red and are marked with a white arrow in the last frame. Images were acquired with a ×10 DIC Fluar objective (NA 0.5) with the following wavelengths for the quantum dots: $\lambda_{ex}=470$ nm; $\lambda_{em}=605/70$ nm. Videos for quantum dots uptake under slow and fast flow conditions are included in Supplementary Movies 1 and 2. **d**, Primary human Kupffer cells were either left untouched, freshly Isolated, or stimulated using a cytokine (stimulated). Cells were then incubated with fluorescent gold nanoparticles for 4 h. (i), (ii), Representative flow plots (i) and histograms (ii) showing the reduction in nanomaterial uptake following stimulation. **e**, The amount of nanomaterial uptake by freshly isolated versus stimulated human Kupffer cells. The values for cells taken from four separate patients are plotted. Statistical significance was evaluated using a two-tailed paired *t*-test (*$P<0.05$).

circulating in the bloodstream slow down by a factor of 1,000 when they enter the liver, increasing the probability for nanomaterial clearance by cells. The amount and rate of cellular uptake is dependent upon each cell's phenotype, internalization and dissociation kinetics, as well as its relative position within the liver microarchitecture. Ultimately, nanomaterials are cleared primarily by Kupffer cells, endothelial cells, B cells and an 'other' cell type. Nanomaterials that do not get taken up leave the organ through the central vein, rejoin the systemic circulation and may return to the liver during a subsequent pass. In this way, the administered hard nanomaterials are cleared from the bloodstream over time.

Outlook

Here we propose an overall mechanism of how hard nanomaterials are cleared by the liver based on the results from our fundamental studies. Future work is required to determine whether the described

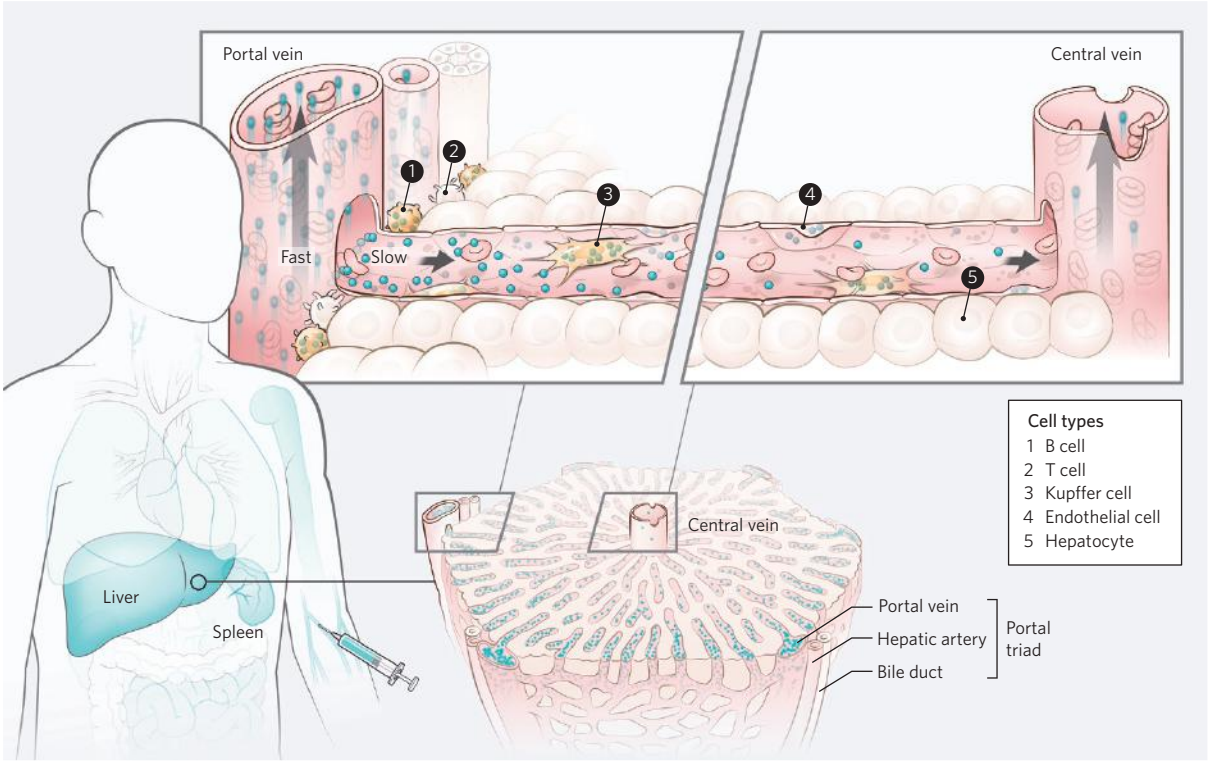

Figure 6 | Mechanism of nanomaterial transport in the liver. Nanomaterials injected into the bloodstream encounter the MPS, a group of organs that contain phagocytic cells. The intensity of the blue colour in the figure reflects the degree of nanomaterial uptake within each MPS organ[12]. As the nanomaterials transition from the peripheral circulation to the liver, their velocity reduces 1,000-fold. This allows the nanomaterials to interact with a variety of cells, resulting in their gradual clearance from the bloodstream. There is a concentration gradient of nanomaterials along the length of the sinusoid, and the amount leaving the liver through the central vein is lower than the amount that enters via the portal triad (see the diagram of liver lobule, bottom right). B and T cells border the portal triad and are exposed to a high concentration of incoming nanomaterials (see the schematic of a liver sinusoid, top). The difference in nanomaterial uptake between these two cell types is due to the increased endocytic/phagocytic capacity of B cells compared with T cells. Nanomaterials that escape the first set of cellular interactions move along the sinusoid and can come into contact with endothelial and Kupffer cells. Hepatocytes are separated from the bloodstream by a layer of fenestrated endothelial cells and do not seem to take up intact hard nanomaterials. Nanomaterials that escape uptake during a pass through the liver return to the systemic circulation via the central vein and are ultimately carried back to the liver (or another MPS organ). This process repeats itself until nanomaterial clearance from the bloodstream is complete.

mechanism can be applied to soft nanomaterials such as micelles and liposomes. The fact that these materials degrade and are deformable adds another interesting facet to how they become cleared from the bloodstream and sequestered by the liver. On the basis of our findings, the solution to the nanomaterial delivery problem will probably combine optimization of nanomaterial design with a pharmaceutical liver pre-conditioning strategy, as suggested by the proof-of-concept data. The liver barrier must be solved to fulfil the promise of using nanomaterials for improving the diagnosis and treatment of human diseases. This study represents the first detailed glimpse into the 'blackbox' and provides a foundation for future studies to improve the targeting efficiency of nanomaterials to diseased tissues.

Received 30 July 2015; accepted 4 July 2016;
published online 15 August 2016

References

1. Kim, B. Y., Rutka, J. T. & Chan, W. C. Nanomedicine. *N. Engl. J. Med.* **363,** 2434–2443 (2010).
2. Veiseh, O., Tang, B. C., Whitehead, K. A., Anderson, D. G. & Langer, R. Managing diabetes with nanomedicine: challenges and opportunities. *Nat. Rev. Drug. Discov.* **14,** 45–57 (2014).
3. Mulder, W. J. M., Jaffer, F. A., Fayad, Z. A. & Nahrendorf, M. Imaging and nanomedicine in inflammatory atherosclerosis. *Sci. Transl. Med.* **6,** 239sr1 (2014).
4. Nasongkla, N. *et al*. Multifunctional polymeric micelles as cancer-targeted, MRI-ultrasensitive drug delivery systems. *Nano Lett.* **6,** 2427–2430 (2006).
5. Jaiswal, J. K., Mattoussi, H., Mauro, J. M. & Simon, S. M. Long-term multiple color imaging of live cells using quantum dot bioconjugates. *Nat. Biotechnol.* **21,** 47–51 (2002).
6. Dhar, S., Daniel, W. L., Giljohann, D. A., Mirkin, C. A. & Lippard, S. J. Polyvalent oligonucleotide gold nanoparticle conjugates as delivery vehicles for platinum(IV) warheads. *J. Am. Chem. Soc.* **131,** 14652–14653 (2009).
7. Kam, N. W. S., O'Connell, M., Wisdom, J. A. & Dai, H. Carbon nanotubes as multifunctional biological transporters and near-infrared agents for selective cancer cell destruction. *Proc. Natl Acad. Sci. USA* **102,** 11600–11605 (2005).
8. Wilhelm, S., Tavares, A. J., Dai, Q., Ohta, S. & Audet, J. Analysis of nanoparticle delivery to tumours. *Nat. Rev. Mater.* **1,** 16014 (2016).
9. Zhang, C. *et al*. Pharmacokinetics, biodistribution, efficacy and safety of N-octyl-O-sulfate chitosan micelles loaded with paclitaxel. *Biomaterials* **29,** 1233–1241 (2008).
10. Fonge, H., Huang, H., Scollard, D., Reilly, R. M. & Allen, C. Influence of formulation variables on the biodistribution of multifunctional block copolymer micelles. *J. Control. Release* **157,** 366–374 (2012).
11. Ye, L. *et al*. A pilot study in non-human primates shows no adverse response to intravenous injection of quantum dots. *Nat. Nanotech.* **7,** 453–458 (2012).
12. Fischer, H. C., Liu, L., Pang, K. S. & Chan, W. C. W. Pharmacokinetics of nanoscale quantum dots: *in vivo* distribution, sequestration, and clearance in the rat. *Adv. Funct. Mater.* **16,** 1299–1305 (2006).
13. Semmler-Behnke, M. *et al*. Biodistribution of 1.4- and 18-nm gold particles in rats. *Small* **4,** 2108–2111 (2008).
14. De Jong, W. H. *et al*. Particle size-dependent organ distribution of gold nanoparticles after intravenous administration. *Biomaterials* **29,** 1912–1919 (2008).
15. Liu, Z. *et al*. *In vivo* biodistribution and highly efficient tumour targeting of carbon nanotubes in mice. *Nat. Nanotech.* **2,** 47–52 (2006).

16. Yang, S. T. *et al*. Biodistribution of pristine single-walled carbon nanotubes *in vivo*. *J. Phys. Chem. C* **111,** 17761–17764 (2007).
17. Hauck, T. S., Anderson, R. E., Fischer, H. C., Newbigging, S. & Chan, W. C. W. *In vivo* quantum-dot toxicity assessment. *Small* **6,** 138–144 (2010).
18. Kuwahira, I., Gonzalez, N. C., Heisler, N. & Piiper, J. Changes in regional blood flow distribution and oxygen supply during hypoxia in conscious rats. *J. Appl. Physiol.* **74,** 211–214 (1993).
19. Fournier, L. S. *et al*. Early modifications of hepatic perfusion measured by functional CT in a rat model of hepatocellular carcinoma using a blood pool contrast agent. *Eur. Radiol.* **14,** 2125–2133 (2004).
20. Miyazaki, S. *et al*. Investigation on the optimal position for the quantification of hepatic perfusion by use of dynamic contrast-enhanced computed tomography in rats. *Radiol. Phys. Technol.* **2,** 183–188 (2009).
21. Menger, M. D., Marzi, I. & Messmer, K. *In vivo* fluorescence microscopy for quantitative analysis of the hepatic microcirculation in hamsters and rats. *Eur. Surg. Res.* **23,** 158–169 (1991).
22. MacPhee, P. J., Schmidt, E. E. & Groom, A. C. Intermittence of blood flow in liver sinusoids, studied by high-resolution *in vivo* microscopy. *Am. J. Physiol. Gastrointest. Liver Physiol.* **269,** G692–G698 (1995).
23. Ingham, D. B. Diffusion of aerosols from a stream flowing through a cylindrical tube. *J. Aerosol. Sci.* **6,** 125–132 (1975).
24. Davies, C. N. Diffusion and sedimentation of aerosol particles from Poiseuille flow in pipes. *J. Aerosol. Sci.* **4,** 317–328 (1973).
25. Dobrovolskaia, M. A. & McNeil, S. E. Immunological properties of engineered nanomaterials. *Nat. Nanotech.* **2,** 469–478 (2007).
26. Lunov, O. *et al*. Differential uptake of functionalized polystyrene nanoparticles by human macrophages and a monocytic cell line. *ACS Nano* **5,** 1657–1669 (2011).
27. Wang, H., Wu, L. & Reinhard, B. M. Scavenger receptor mediated endocytosis of silver nanoparticles into J774A.1 macrophages is heterogeneous. *ACS Nano* **6,** 7122–7132 (2012).
28. Sykes, E. A., Chen, J., Zheng, G. & Chan, W. C. W. Investigating the impact of nanoparticle size on active and passive tumor targeting efficiency. *ACS Nano* **8,** 5696–5706 (2014).
29. Perrault, S. D., Walkey, C., Jennings, T., Fischer, H. C. & Chan, W. C. W. Mediating tumor targeting efficiency of nanoparticles through design. *Nano Lett.* **9,** 1909–1915 (2009).
30. Cho, W.-S. *et al*. Size-dependent tissue kinetics of PEG-coated gold nanoparticles. *Toxicol. Appl. Pharmacol.* **245,** 116–123 (2010).
31. Chithrani, B. D. & Chan, W. C. W. Elucidating the mechanism of cellular uptake and removal of protein-coated gold nanoparticles of different sizes and shapes. *Nano Lett.* **7,** 1542–1550 (2007).
32. Gao, H. J., Shi, W. D. & Freund, L. B. Mechanics of receptor-mediated endocytosis. *Proc. Natl Acad. Sci. USA* **102,** 9469–9474 (2005).
33. Cormode, D. P. *et al*. A versatile and tunable coating strategy allows control of nanocrystal delivery to cell types in the liver. *Bioconjug. Chem.* **22,** 353–361 (2011).
34. Cheng, S.-H. *et al*. Visualizing dynamics of sub-hepatic distribution of nanoparticles using intravital multiphoton fluorescence microscopy. *ACS Nano* **6,** 4122–4131 (2012).
35. Akinc, A. *et al*. Targeted delivery of RNAi therapeutics with endogenous and exogenous ligand-based mechanisms. *Mol. Ther.* **18,** 1357–1364 (2010).
36. Sadauskas, E. *et al*. Kupffer cells are central in the removal of nanoparticles from the organism. *Part. Fibre Toxicol.* **4,** 10–17 (2007).
37. Bartneck, M. *et al*. Peptide-functionalized gold nanorods increase liver injury in hepatitis. *ACS Nano* **6,** 8767–8777 (2012).
38. Nakashima, M. *et al*. Pivotal advance: characterization of mouse liver phagocytic B cells in innate immunity. *J. Leukoc. Biol.* **91,** 537–546 (2012).
39. Stock, R. J., Cilento, E. V., Reilly, F. D. & McCuskey, R. S. A compartmental analysis of the splenic circulation in rat. *Am. J. Physiol. Heart Circ. Physiol.* **245,** H17–H21 (1983).
40. Chadburn, A. The spleen: anatomy and anatomical function. *Semin. Hematol.* **37,** 13–21 (2000).
41. Delp, M. D., Evans, M. V. & Duan, C. Effects of aging on cardiac output, regional blood flow, and body composition in Fischer-344 rats. *J. Appl. Physiol.* **85,** 1813–1822 (1998).
42. Walkey, C. D., Olsen, J. B., Guo, H., Emili, A. & Chan, W. C. W. Nanoparticle size and surface chemistry determine serum protein adsorption and macrophage uptake. *J. Am. Chem. Soc.* **134,** 2139–2147 (2012).
43. Jones, S. W. *et al*. Nanoparticle clearance is governed by Th1/Th2 immunity and strain background. *J. Clin. Invest.* **123,** 3061–3073 (2013).
44. Koo, A., Liang, I. Y. & Cheng, K. K. Hepatic sinusoidal responses to intraportal injections of phenylephrine and isoprenaline in the rat. *Clin. Exp. Pharmacol. Physiol.* **3,** 391–395 (1976).
45. Hagemann, T. *et al*. 'Re-educating' tumor-associated macrophages by targeting NF-B. *J. Exp. Med.* **205,** 1261–1268 (2008).

Acknowledgements

We would to acknowledge the Canadian Institute of Health Research, Natural Sciences and Engineering Research Council, and Collaborative Health Research Program for funding the project. K.M.T. thanks the NSERC Vanier Canada Graduate Scholarship Program and the Surgeon-Scientist Program at the University of Toronto for financial support. S.A.M. thanks the CASL/CIHR Hepatology Fellowship Program and the National CIHR Research Training Program in Hepatitis C for financial support. We would also like to acknowledge M. Peralta and C. Hoculada from the University Health Network Pathology Research Program (Toronto, Canada), D. Holmyard from the Mount Sinai Advanced Bioimaging Centre (Toronto, Canada), F. Xu from the University Health Network Advanced Optical Microscopy Facility (Toronto, Canada), D. White from the Department of Immunology, University of Toronto (Toronto, Ontario), J. Manual, J. Feld and V. Cherepanov from the Toronto Centre for Liver Disease (Toronto, Canada), J. Krieger from the SPARC Biocentre at the Hospital for Sick Children (Toronto, Canada) and A. Black from the Department of Anatomy, National University of Ireland, Galway (Galway, Ireland) for their assistance.

Author contributions

K.M.T., S.A.M., J.B.C., I.D.M. and W.C.W.C. conceived the idea. K.M.T., S.A.M., O.A.A., I.D.M. and W.C.W.C. analysed the data. K.M.T. and S.A.M. conducted the experiments with assistance from X.-Z.M., V.N.S., J.E., B.O., S.M.F., E.A.S., N.G. and J.M.K. A.Z. performed the mathematical modelling. B.A.A., M.S. and M.A.O. supervised some of the work.

Additional information

Supplementary information is available in the online version of the paper. Reprints and permissions information is available online at www.nature.com/reprints. Correspondence and requests for materials should be addressed to I.D.M. or W.C.W.C.

Competing financial interests

The authors declare no competing financial interests.